

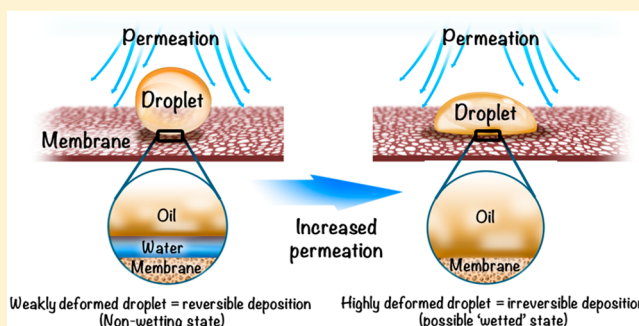
Microscale Dynamics of Oil Droplets at a Membrane Surface: Deformation, Reversibility, and Implications for Fouling

Gali Fux and Guy Z. Ramon*^b

Department of Civil & Environmental Engineering, Technion - Israel Institute of Technology, Haifa, Israel 32000

S Supporting Information

ABSTRACT: Despite their excellent capabilities, wide implementation of membranes for oil/water emulsion separation is limited due to severe fouling. To date, microscale dynamics of the oil–water–membrane system are poorly understood. The present study uses confocal microscopy at unprecedented resolution for direct observation of oil droplet deposition, deformation, and detachment during separation and cleaning, respectively. The 3D shape of the droplets was imaged as a function of the permeation rate, J , droplet radius, R , membrane permeance, k , water viscosity, μ , and the water/oil interfacial tension coefficient, σ . These parameters yield a modified capillary number, $\widehat{Ca} = \mu VR^{1/2}/\sigma k^{1/2}$, which accounts for the extra viscous “suction” at close proximity to the membrane surface. A clear correlation was observed between the degree of droplet deformation and an increasing \widehat{Ca} . Furthermore, the reversibility of droplet deposition and membrane performance were assessed through microscopic surface coverage and flux recovery analysis. In general, operation at a low flux ($3.9 \mu\text{m/s}$) yields spherical droplets that are easily removed by crossflow cleaning, whereas a high flux ($85 \mu\text{m/s}$) leads to significant deformation and mostly irreversible deposition. These results shed important new insight on the influence of hydrodynamic conditions on fouling reversibility during emulsion separation, and may guide better design of surface-modified membranes.



1. INTRODUCTION

Oily wastewater is a byproduct of many industrial processes.¹ A particularly important source is due to extraction of unconventional oil and gas, which generates increasing volumes of “produced water”.^{2,3} In order to meet regulation levels (typically 15–40 mg/L^{4,5}) extensive treatment is required.⁶ However, most methods are limited to removal of free-floating and unstable oil, whereas stable oil, in the form of emulsified droplets smaller than $20 \mu\text{m}$,⁷ is not effectively removed by traditional methods.⁸ The challenge of separating stable emulsions has been met by membranes; however, fouling and the resulting loss of performance remain a problem in the large-scale implementation of this technology.^{4,9,10} In general, hydrophilic membranes are more resistant to fouling and have been widely investigated.^{5,11–14} Many efforts are currently focused on fabricating superoleophobic–superhydrophilic surfaces, where the probe liquid contact angle is greater than 150° (for oil) or smaller than 10° (for water).^{7,15,16}

Despite the efforts to improve membranes antifouling properties, there is a lack of fundamental, mechanistic knowledge regarding the early stages of oil droplet deposition on the membrane surface during separation.⁵ Oil droplets tend to easily deform, break up, and coalesce in a complicated way that may affect the fouling characteristics. For instance, blocking laws, which are often used as models to describe fouling mechanisms in filtration systems, were formulated for solid particles in suspensions,¹⁷ which are expected to behave

differently than liquid–liquid, emulsified systems.⁴ To date, most studies have been focused on experimentally assessing the success of surface modifications via indirect measures, such as flux decline and oil rejection,^{18–21} with very few studies aimed at understanding the dynamics of droplets at a permeable surface, its dependence on controllable parameters such as trans-membrane pressure, pH, surfactant concentration, and their influence on the energy demand and product quality.²²

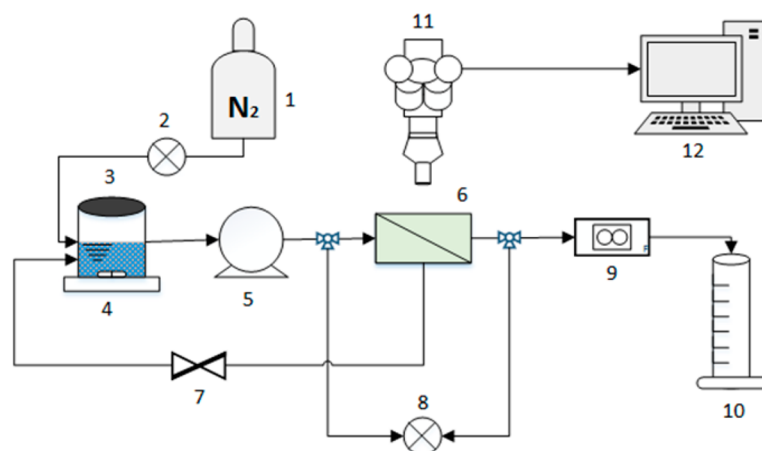
Direct microscopic observation during separation can provide important insight into the actual phenomena occurring at the membrane surface, and has been successfully employed in recent years for noninvasive monitoring of particulate and microbial deposition and fouling.^{23–26} However, in the case of oil fouling, such studies are scarce. In a recent paper, Tummons et al.²² studied the dynamics of oil droplets on Anopore and track-etched microfiltration membranes, which become transparent when wet and allow bright-field imaging. Their study identified three characteristic stages of membrane fouling by oil: (1) droplet attachment and clustering, (2) axial droplet deformation, and (3) droplet coalescence. Although these stages were clearly noticeable, most of the small, stable droplets (with a diameter of $1–10 \mu\text{m}$) did not seem to fit these criteria,

Received: July 4, 2017

Revised: October 7, 2017

Accepted: November 6, 2017

Published: November 7, 2017



System components: (1) Gas tank (2) Pressure gauge (3) Sealed feed vessel (4) Magnetic stir plate (5) Gear pump (6) Flow cell (7) 2-way valve (8) Differential pressure transducer (9) Flow rate sensor (10) Permeate tank (11) Confocal microscope (12) Computer

Figure 1. Schematic diagram of the experimental system. The filtration process was conducted in a dead-end configuration. Monitored by an applied pressure gauge, a differential pressure transducer, and a flow rate sensor, emulsion was pumped from the feed vessel to the flow cell at the desired permeate flux. The membrane surface was continuously observed via a glass window on the flow cell by a laser-scanning confocal microscope.

but rather remained stable as clusters on the membrane. The droplets that appeared to coalesce may already be considered unstable and large ($>20 \mu\text{m}$) when reaching the surface, consistent with an “Ostwald ripening” mechanism.²⁷ In a continuing work by the same group,²⁷ the additional effects of surfactant and divalent cations on fouling were studied. Two factors were shown to promote droplet coalescence: permeate drag, which increased the residence time of droplets on the membrane surface, and high ionic strength of divalent cations, which characterizes produced water effluents. It was further suggested that coalescence primarily took place within the crossflow channel and not on the membrane surface, since the droplets that were observed depositing on the surface were larger than those in the bulk, which means the droplets that reached the surface were large and unstable to begin with. To date, the influence of pressure and hydrodynamics on the three-dimensional shape of a droplet interacting with a membrane had been investigated only theoretically, and with emphasis placed on pore-scale effects and tangential shear.^{28–30}

It is, therefore, the purpose of this paper to present the dynamics of small, “stable” droplets at a membrane surface and, specifically, the effect of permeate flux, droplet size, and membrane permeance on droplet shape and extent of deformation. Furthermore, the relation between droplet deformation and fouling reversibility was examined and implications for further process development are discussed based on the new mechanistic insight.

2. MATERIALS AND METHODS

2.1. Membranes. The membranes used are commercial, flat sheet poly(ether sulfone) (PES) ultrafiltration (UF) membranes (Synder filtration), with a molecular weight cutoff of either 10 kDa (“ST”) or 100 kDa (“LY”). Prior to each experiment, the membrane’s pure water permeance was characterized by applying a gradual pressure variation and measuring the permeate flow in dead-end mode, from which the permeance, $L_p = Q/A\Delta P$, was calculated, where Q is the permeate flow (m^3/s) measured by a sensitive flow sensor (Mitos Flow Rate Sensor, Dolomite Ltd., Norwell, MA, USA), A is the effective membrane filtration area (m^2), and ΔP is the

trans-membrane pressure, measured by a differential pressure transducer (PX409, Omega Engineering, Bridgeport, NJ, USA). The average permeability measured was $1.2 \times 10^{-10} \frac{\text{m}}{\text{s}\cdot\text{Pa}}$ (ST) and $2.3 \times 10^{-10} \frac{\text{m}}{\text{s}\cdot\text{Pa}}$ (LY); in all experiments, only membranes with a permeability within 10% of these average values were used.

2.2. Oil–Water Emulsion Preparation and Characterization. Hexadecane (99%) and Triton X-100 (henceforth referred to as “triton”) were purchased from Sigma-Aldrich Co., USA. Deionized (DI) water was supplied by a Milli-Q ultrapure water device. The oil/water emulsion was prepared as follows: $20 \mu\text{L}$ of hexadecane stained with 1% Dye-Lite (Fluorescence Dye, 561 nm excitation, Tracerline, USA) were mixed with 200 mL of DI water containing Triton (1:10 surfactant/oil v/v ratio). The mixture was sonicated for 3 min in an ultrasonic bath (MRC laboratory instruments Inc., Israel). The size distribution of the oil droplets was measured using a light scattering particle size analyzer (Malvern Mastersizer, Malvern Instruments Ltd., UK). The contact angle of hexadecane on the “LY” membrane surface was measured in both DI water and a $5 \times 10^{-5} \text{ M}$ triton solution, using the captive drop method with an external contact angle measurement setup (Dataphysics OCA 15Pro., Germany). Oil/water/triton interfacial tension was measured using the pendant drop method with the same setup as the contact angle measurement. The water–triton viscosity was measured with a discovery hybrid rheometer (TA Instruments, USA).

2.3. Experimental System. The experimental setup is shown schematically in Figure 1. A custom-made crossflow membrane filtration cell, fitted with a sapphire glass window enabling optical access, was used for visualization experiments. Channel dimensions within the cell are 0.6 mm (H) \times 6 mm (W) \times 36 mm (L) with a total membrane filtration area of 216 mm^2 . The flow cell is mounted on the fixed stage of an inverted, laser-scanning confocal microscope (Leica TCS SP8, Leica Microsystems, Wetzlar, Germany) equipped with a long-working distance, water-immersion, 25 \times objective with a numerical aperture of 0.95, enabling high resolution. The sealed feed vessel and the entire system were placed under a

static background pressure applied through compressed Nitrogen. In each experiment, a fixed permeate flux was maintained by adjusting the applied pressure. The permeate flow rate was measured using an ultralow flow sensor (Mitos Flow Rate Sensor, Dolomite Ltd., Norwell, MA, USA). Transmembrane pressure was measured with a differential pressure transducer (PX409, Omega Engineering, Bridgeport, NJ, USA), connected to the feed and permeate tubing before and after the cell. The emulsion was kept stirred within the feed tank at 400 rpm using a magnetic stirrer plate. In the cross-flow stage during the deposition and release experiments, DI water was pumped through the cell under zero applied pressure using a programmable gear pump (Micropump, Cole Parmer, Vernon Hills, IL, USA).

2.4. Deformation Experiments. The deformation experiments proceeded along the following protocol. A fresh membrane coupon was placed in the flow cell at the start of each experiment. First, the pure water permeability was determined as described in section 2.1. This was followed by pumping a 100 mg/L oil–water emulsion at zero applied pressure, to fill the flow cell and tubing with feed solution. Then, the feed tube was connected to a second, pressurized tank containing DI water, where the pressure was set to obtain the desired permeate flux. The feed change to DI water was made to prevent additional droplet deposition on the surface. Five permeate fluxes were tested: $J = 2.3, 3.9, 15, 54,$ and $85 \mu\text{m/s}$. The lowest flux was chosen based on preliminary experiments, where it was observed that lack of permeate flux causes the droplets to vibrate noticeably, presumably due to Brownian motion, on the membrane surface. In order to scan the droplet at different planes accurately, it must remain stable upon the surface. This was only achieved under a flux of $2.3 \mu\text{m/s}$. Once the pressure was applied, oil droplets began to deposit on the membrane surface and image acquisition commenced. In order to isolate the effect of permeation over crossflow shear, which was shown theoretically and experimentally to effect the shape of droplets on the membrane surface,^{22,30} these experiments were conducted in dead-end mode. For each permeate flux, experiments were performed in triplicate, where, in each repetition, 50 droplets from different locations on the membrane surface were scanned. In high flux experiments (54 and $85 \mu\text{m/s}$), this was followed by reduction of the permeate flux to 0, after which the droplets were scanned again.

2.5. Image Acquisition and Analysis. During a deformation experiment, droplets with the desired diameter ($5/10/15 \pm 1 \mu\text{m}$) were first located on the membrane surface and magnified so as to acquire higher scan performance and resolution, as well as reduced background noise. Then, a scan of each droplet at different focal planes, top to bottom, was performed, with step sizes of $0.33 \mu\text{m}$ in the vertical direction. The excitation wavelength of the fluorescent dye is 561 nm , and both reflected light and fluorescent light were detected, representing the nonfluorescent membrane surface and the red-dyed oil droplets, respectively. Each droplet position on the surface was marked so that they would be imaged only once. Image analysis was then performed with a three-dimensional reconstruction software (IMARIS, Bitplane, Oxford Instruments, UK), providing the droplets' physical dimensions and volume. Calibration of lateral to axial resolution was performed with $15 \mu\text{m}$ microspheres (Probes' Focal Check); for details of this procedure please refer to the Supporting Information.

The deformation factor, used to quantify the degree of deformation, is here defined as

$$D_f = \frac{Z}{d}$$

where

$$d = \left(\frac{6V}{\pi}\right)^{1/3}$$

in which V is the droplet volume, Z is the vertical length of the droplet, both of which are provided by the image analysis, and d is the calculated diameter of the undeformed droplet diameter (see an example of the full calculation procedure presented schematically in Figure 2). This factor was chosen for its clear

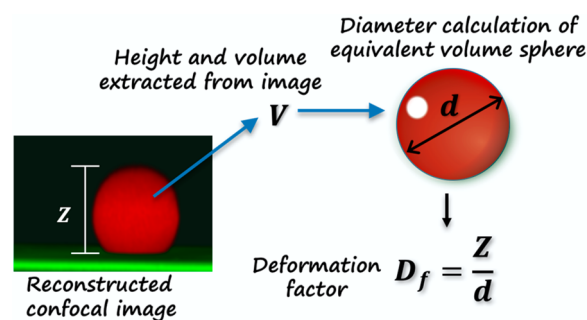


Figure 2. Example calculation of the deformation factor, D_f . The image analysis software provides the physical dimensions of each scanned droplet. Specifically, the vertical height of the droplet, Z , is measured, as is V , its volume, which is then used to infer the diameter of the initial, undeformed (spherical) droplet. The deformation factor is the ratio of the droplet height to the initial diameter, i.e. Z/d .

and simple physical meaning, where one may imagine the droplet's compression from an initial sphere. In each experiment, 50 droplets were scanned, and the average deformation factor and standard deviation were calculated (see details of these in the Supporting Information).

2.6. Deposition and Release Experiments. The deposition and release experiments followed the same initial part of the deformation protocol, except that a higher oil–water emulsion concentration (200 mg/L) was used. The emulsion was filtered for 20 min at two fluxes: $3.9 \mu\text{m/s}$ (“Low flux”) and $85 \mu\text{m/s}$ (“High flux”). At the end of the filtration, ten images of a $120 \mu\text{m} \times 120 \mu\text{m}$ area were acquired, from which the surface coverage (SC) and surface coverage recovery (SCR) were calculated with Leica analysis software (Leica SP8) using the following definitions:

$$\text{SC} = \frac{A_o}{A_t}$$

where A_o is the projected membrane area covered by oil droplets and A_t is the total membrane surface area viewed under the microscope. In a similar manner, we define

$$\text{SCR} = 1 - \frac{\text{SC}_a}{\text{SC}_b}$$

in which the subscripts b and a denote before and after the cleaning step, respectively. Following the oil deposition, crossflow cleaning was applied for 2 min. The crossflow velocity was 0.05 m/s , corresponding with a Reynolds number, $Re \approx 2\rho UH/\mu = 30$ where ρ is the water density, U is the bulk

Table 1. Characteristics of the UF PES Membranes and Hexadecane/Water/Triton X-100 Emulsion

| Hexadecane/membrane contact angle (deg) | Viscosity (Pa·s) | Interfacial tension (N/m) | Size distribution (μm) | Average droplet size (μm) | Permeability (m/s·Pa) |
|--|--------------------------|---|------------------------|---------------------------|---|
| 108 ± 2 (in water) | 1.9 × 10 ⁻³ ± | 1.2 × 10 ⁻² ± 5 × 10 ⁻³ | 0.8–50 | 5.5 | 1.2 × 10 ⁻¹⁰ (ST) ^a |
| 110 ± 1 (in 5 × 10 ⁻⁵ M triton) | 1.36 × 10 ⁻⁴ | | | | 2.3 × 10 ⁻¹⁰ (LY) ^a |

^aAll membranes used were within 10% of these values, in all experiments.

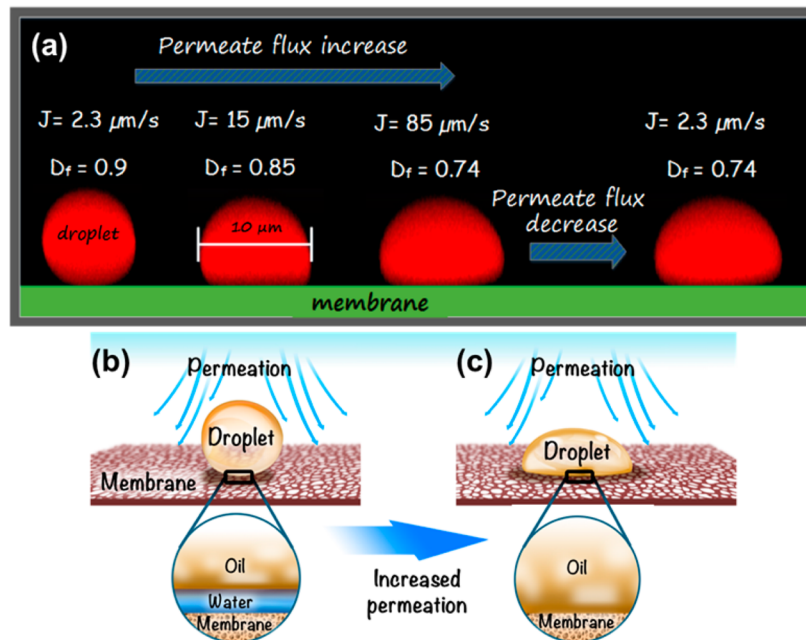


Figure 3. (a) Representative confocal images showing degrees of oil droplet deformation ($R = 5 \mu\text{m}$) in response to increased and decreased permeate flux. (b) Conceptual schematic of the “stable” water film trapped between the oil droplet and the membrane surface. (c) Increased permeation induces drainage and rupture of the water film, and a transition to wetting of the membrane by the oil.

cross-flow velocity, H is the channel height, and μ is the feed viscosity. Following the cleaning step, a second round of image acquisition took place as detailed above. These experiments were conducted for LY membranes only and included at least three repetitions for each permeate flux. In order to further evaluate the efficiency of membrane cleaning, the flux recovery ratio (FRR) was calculated using the following expression:

$$\text{FRR} = \frac{J_0}{J_a}$$

where J_0 is the initial water flux at the given applied pressure and J_a is the water flux obtained for the same pressure, after emulsion filtration and crossflow cleaning. A higher FRR value means better cleaning efficiency.

3. THEORETICAL CONSIDERATIONS

Deformation of droplets in viscous flows is a widely investigated topic, both experimentally and theoretically.^{31–33} In general, the degree of deformation is related to the capillary number

$$\text{Ca} = \frac{\mu V}{\sigma}$$

where V is a characteristic velocity and σ is the interfacial tension. This dimensionless parameter embodies the ratio of viscous stresses generated by the fluid motion, which tend to deform the droplet, and interfacial tension which tends to minimize the surface area and keep the droplet spherical, hence

resisting deformation. However, in the case considered here, the droplet is in close proximity to a permeable surface (the membrane), and this proximity modifies the viscous stresses. Previous work has shown that, close to a permeable boundary, the viscous “suction” can greatly exceed the force expected under similar fluid velocities in an unbounded fluid.^{34–36} In general, for a spherical particle, the viscous force scales as $\sim \mu V R^{3/2} / k^{1/2}$, with R as the radius of the particle and $k = L_p / l_m$ the membrane permeance, which is the membrane permeability per unit thickness. Note that permeance here is independent of the fluid (as used in the porous media literature) and is the reciprocal of the membrane resistance.

Next, we use this force scaling to adjust the capillary number to the problem studied. Again, using the ratio of the viscous and surface tension forces, a modified capillary number is now defined as

$$\widehat{\text{Ca}} = \frac{\mu J}{\sigma} \left(\frac{R}{k} \right)^{1/2}$$

where J , the permeate flux, represents the system characteristic velocity. This number reflects the fact that, at close proximity to the membrane, droplet size and the membrane permeance are expected to strongly affect the viscous force on the droplet and, thus, the tendency of a droplet to deform. We therefore anticipate that this number will enable the estimation of deformation propensity through a single dimensionless parameter, which embodies the emulsion, membrane, and operational characteristics, thereby simplifying the analysis. It is

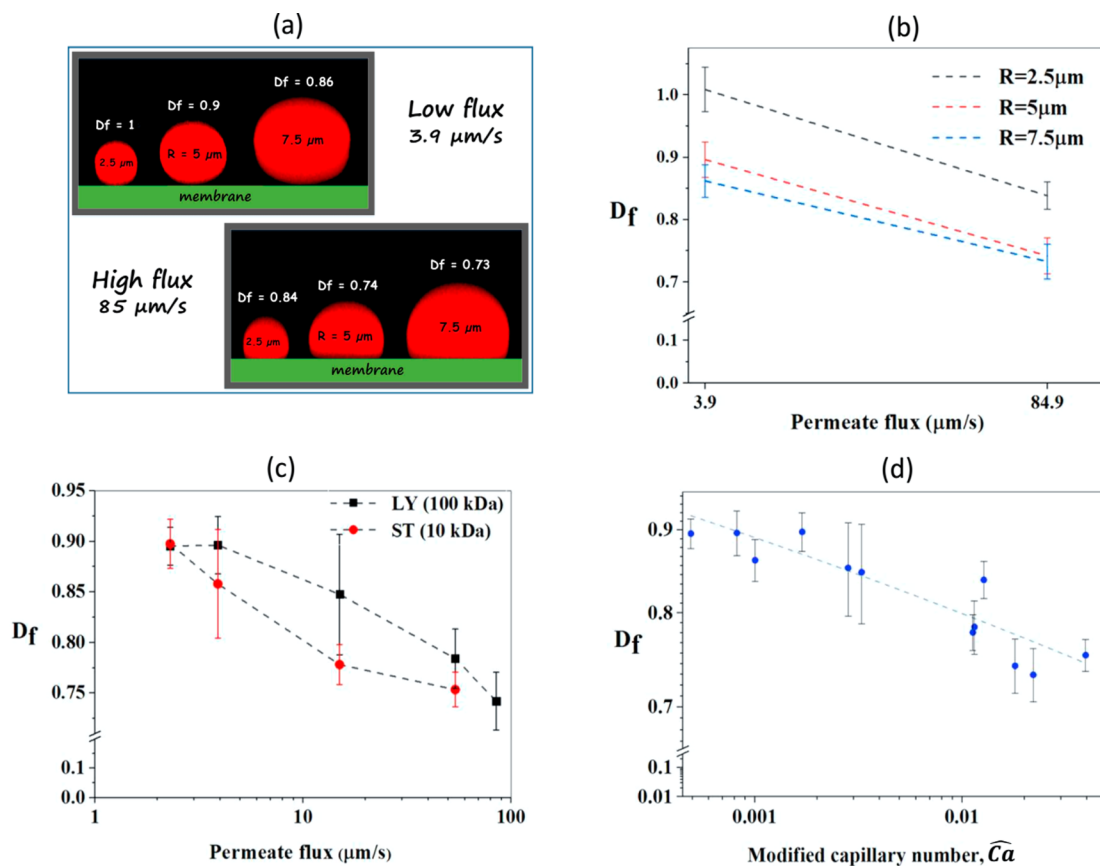


Figure 4. Deformation factor, $D_f = z/d$, under different experimental conditions. (a and b) Effect of droplet size ($R = 2.5, 5, 7.5 \mu\text{m}$) under two permeate fluxes ($J = 3.9, 85 \mu\text{m/s}$). (c) Effect of membrane permeance for two membranes (“ST”: 10 kDa, “LY”: 100 kDa) and varying permeation rates. (d) Summary of all deformation results, as a function of a single dimensionless parameter - the modified capillary number $\widehat{Ca} = \mu J R^{1/2} / \sigma k^{1/2}$.

noted that two important assumptions are built into this simple analysis: flow within the droplets is neglected, and their shape is assumed to be spherical. The former is likely a good approximation for a surfactant-stabilized droplet, which renders the interface immobile; the second assumption is an obvious error, as these droplets do not retain their spherical shape.

4. RESULTS AND DISCUSSION

4.1. Droplet Deformation at the Membrane Surface Due to Permeation. The emulsion characteristics are summarized in Table 1 (further information on size distribution and contact angle may be found in the Supporting Information). The underlying hypothesis of this work is that oil droplets deform at the membrane surface, and this deformation is a function of the permeate flux, J , droplet radius, R , and membrane permeance, k , which may be combined to produce the modified capillary number, $\widehat{Ca} \equiv \mu J R^{1/2} / \sigma k^{1/2}$. The permeate flux is a key parameter in controlling fouling as well as oil droplet rejection.³⁷ Results indicate that by increasing the permeate flux, oil droplets deform from an almost perfect sphere to nearly a hemisphere (see Figure 3a). Based on the shape and contact angle of an oil droplet on the membrane surface under static conditions (see Table 1 and Supporting Information) it is clear that the membrane is hydrophilic. Comparing these with images under low flux filtration conditions, it appears that the droplet becomes even more spherical. This might be due to an existence of a stable thin water film between the droplet and the membrane surface (see illustration in Figure 3b) through which

a continuous flow of water into the membrane pores is maintained, preventing the oil from wetting the membrane. However, as the flux is increased, so does the viscous “suction” force pressing the droplet toward the membrane, eventually draining the thin water film to the point where it may destabilize, resulting in the adherence of the oil to the membrane (shown schematically in Figure 3c). As illustrated in Figure 3a, deformation increases, concurrently with the flux, but then remains constant even upon dramatic reduction of the flux.

Droplet size affects deformation propensity. Droplets in three size categories: $R = 2.5, 5, 7.5 \mu\text{m}$, were imaged under two permeate fluxes, $J = 3.9, 85 \mu\text{m/s}$ with the more permeable LY membrane only (see Figure 4a, b). The effect of the droplets size on the corresponding deformation is significant. At the low permeate flux, small droplets remained spherical, medium droplets deformed slightly, and big droplets experienced the highest deformation: $D_f = 1, 0.9, 0.86$ for $R = 2.5, 5, 7.5 \mu\text{m}$, respectively. For the high permeate flux the trend was identical, but with only a slight difference between big and medium droplets ($D_f = 0.84, 0.74, 0.73$ for $R = 2.5, 5, 7.5 \mu\text{m}$, respectively). This also suggests that deformation may “saturate”, that is, reach a finite value beyond which further increasing the permeation will not incur additional deformation.

Deformation is greater for a low permeance membrane. Experiments were conducted using two membranes with different permeances (see Table 1 for membrane properties) under several permeate fluxes. As shown in Figure 4c, for both

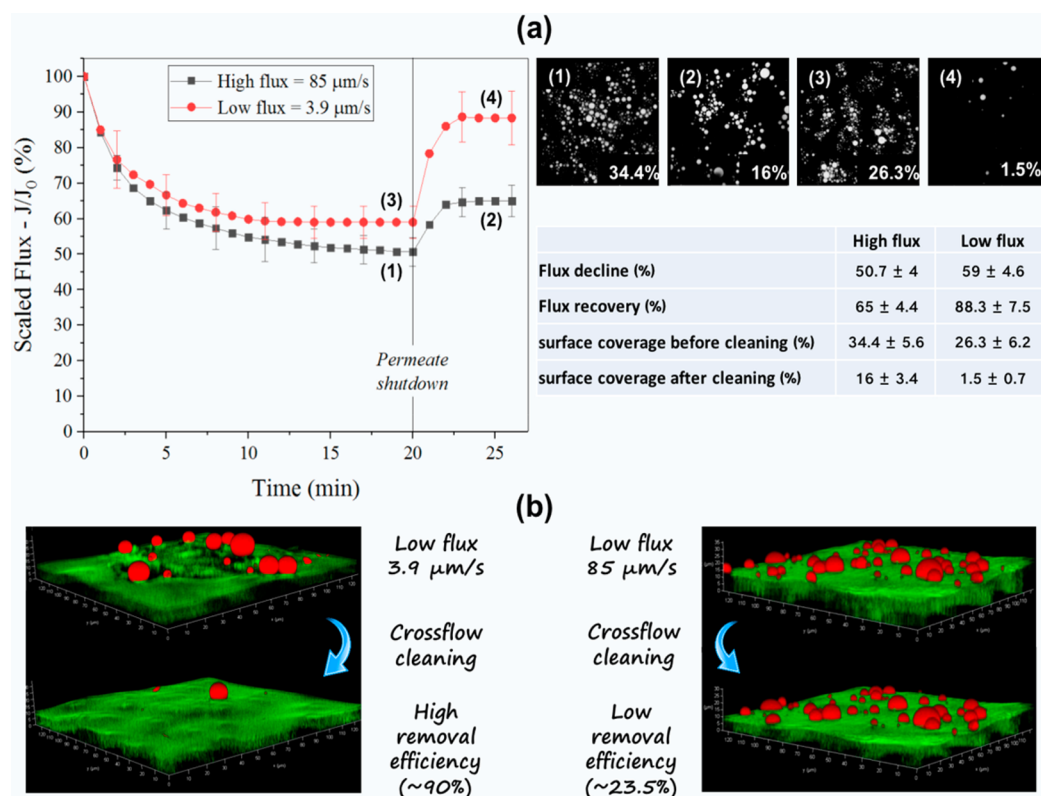


Figure 5. (a) Changes in the flux, scaled against the initial flux, during emulsion separation at “High” ($J = 85 \mu\text{m/s}$) and “Low” ($J = 3.9 \mu\text{m/s}$) fluxes, followed by crossflow cleaning and pure water filtration, from which a flux recovery ratio (FRR) was calculated. Also shown are images illustrating the surface coverage (SC) at different times, before and after cleaning. These are marked as (1)–(4) corresponding with the labels on the flux decline curve. (b) Representative confocal images of the membrane surface, before and after cleaning, following separation under high or low flux conditions. Under low flux, most droplets appear spherical and were easy to remove by crossflow cleaning, whereas under the high flux droplets were mostly deformed and remained attached to the membrane, while only some of the small droplets were removed by crossflow.

membranes, deformation is already measured at the lowest flux ($D_f = 0.897$ for ST and $D_f = 0.9$ for LY, at $J = 2.3 \mu\text{m/s}$). The deformation then increases markedly at a low flux for the less permeable, ST membrane. The largest deformation observed for both membranes is practically identical, 0.742 for LY and 0.753 for ST, but is obtained at different fluxes. This observation suggests, again, that the deformation “saturates” and does not increase beyond a limiting value.

The effect of membrane permeance is clearly manifested: for a less permeable membrane, higher deformation is induced at the same flux. The relatively large error bars for $J = 3.9 \mu\text{m/s}$ with ST and $J = 15 \mu\text{m/s}$ with LY reflect the statistical nonuniformity of the droplets at those fluxes: some were spherical while others were deformed. We believe this is indicative of the membrane heterogeneity: deformation is dictated by the local flux and local permeance, which may vary quite widely on the microscale (for example, due to pore size distributions and pore clusters), while the measured flux and permeance are averaged over the entire membrane area used. These fluxes may be considered as “transitional fluxes”, in the sense that, below them, all droplets are relatively spherical and, above them, all droplets are deformed, to different extents.

Modified Capillary Number. Theoretical considerations of the force balance near the membrane surface have led us to believe that the tendency of droplets to deform, though shown to depend on the permeate flux, droplet size, and membrane permeance, may be described using a single dimensionless parameter, \widehat{Ca} . This point is illustrated in Figure 4d where all

the deformation results are plotted against \widehat{Ca} and demonstrate a clear correlation between droplets deformation from a sphere to an approximate hemisphere in response to increasing the modified capillary number. Since we have shown that deformation is linked to wetting and irreversible fouling, this parameter reduces the number of experiments necessary for one to determine the propensity for a given system to foul. However, we also note that this parameter is based on a simplified force balance that does not fully capture the complexity of the problem; for example, the viscous force on the droplet increases as it deforms.³⁶ Therefore, we cannot suggest, at this point, the existence of a “scaling law”. The “saturation” of the deformation may be due to hydrodynamic “pinning” that limits the spreading of the droplet, or may be a simple consequence of the threshold pressure required to squeeze the droplet through the membrane; approaching this pressure could mean that part of the droplet begins to protrude into the membrane pores. Indeed, our observations have been that, for the higher pressure system (the less permeable membrane) at the “saturation” point, a further increase of the applied pressure can indeed result in the droplet passing through the membrane.

4.2. Implications for Fouling. In a final set of experiments, the relation between droplet deformation and larger-scale fouling reversibility was examined. The degree of fouling reversibility is determined by the ability to remove deposited material from the membrane surface and pores, thereby restoring initial performance. Irreversible fouling is here

considered to be such that physical cleaning cannot detach the droplets,^{38,39} leading to low flux recovery and loss of membrane performance. For simplicity, crossflow cleaning, a hydraulic rinsing strategy,⁴⁰ was applied.

Figure 5b presents images of droplets' shape before and after crossflow cleaning, applied after separation under two fluxes ("low" = 3.9 $\mu\text{m/s}$, "high" = 85 $\mu\text{m/s}$), at two spatial scales that allow a representation of surface coverage effects while also considering individual droplet shape. As shown in section 3, under low permeate flux the droplets remain spherical, whereas under high flux the droplets deform. Cross-flow cleaning successfully removed the spherical droplets from the membrane surface, whereas deformed ones remained attached to the surface. These results correspond with those reported by Tummons et al.,²⁷ whereby in the absence of permeation, some of the droplets that deposited on the membrane could be removed by crossflow. This was not seen under permeation conditions. Figure 5a also presents the flux changes and surface coverage during filtration and following crossflow cleaning. Since the system is operated in dead-end mode, the flux initially declined dramatically under both fluxes, due to deposition of oil droplets, presumably at areas of the largest local permeance. This was followed by a more moderate flux decline stage with a possible stabilization under the low flux conditions. After crossflow cleaning, the FRR and SCR were much higher for the low-flux filtration (see the table in Figure 5a for a summary of these results). The only droplets that were removed from the surface after high flux filtration were small droplets ($R < 2.5 \mu\text{m}$), which corresponds well with our single-droplet results that showed small droplets barely deform even under high flux conditions (see section 3).

Based on this study, we propose that a critical flux of oil fouling exists, but its "criticality" must be considered in a slightly different manner compared with the classical definition of deviation from the pure water line.⁴¹ Our result better corresponds with the second definition of the critical flux, which is the permeate flux for which irreversible fouling appears on the membrane.^{39,42} The presented results demonstrate that oil fouling is not just dependent on the deposition of a droplet, but also on whether the droplet deforms, and to what extent. We have shown that the deformation propensity correlates with a modified capillary number that embodies the combined effect of the emulsion characteristics (viscosity, surface tension, droplet size) as well as process conditions (the membrane used and the permeate flux). In the case considered here, the membrane surface appears to be preferentially wetted by the aqueous phase (as determined through static contact angle measurements), but under the influence of viscous suction a transition occurs that leads to wetting of the membrane by the oil droplet. We speculate that this transition is linked to the drainage and eventual destabilization and rupture of a water film that initially separates the droplet from the surface. This idea is based on established theories of droplet coalescence in liquid–liquid systems, here extended to a solid–liquid case. The stability of the liquid film dictates the transition from a nonwetting to a wetting state, akin to a transition from a Cassie–Baxter state to a Wenzel state; such a transition cannot be ruled out in this case, since there is some (small) surface heterogeneity (solid vs liquid patches) and roughness. The transition threshold from a nonwetting and, therefore, reversible state to a wetted, irreversible state also depends on surface chemistry and attractive surface potentials between the oil and the membrane, as well as electrostatic repulsion, though

the latter can be very weak in a system stabilized by a nonionic surfactant,⁴³ as considered here. For membranes that are more hydrophilic/underwater-oleophobic than PES (for instance, polyacrylonitrile, cellulose acetate, etc.), and especially rough membranes, the transition threshold flux is expected to be higher than the one observed in the present study, which constituted a relatively low operational flux for UF membranes. Finally, an important point to consider, based on these results, is that static contact angle measurements provide a very gross estimate of a given membrane/oil system's tendency to undergo irreversible fouling, due to the dynamic nature of the wetting process illustrated here. Future work will include more specific attention to the effect of surface interactions on the permeation-induced transition to wetting, and its implications for fouling control.

■ ASSOCIATED CONTENT

§ Supporting Information

The Supporting Information is available free of charge on the ACS Publications website at DOI: 10.1021/acs.est.7b03391.

Details of microscopy and image analysis, droplet deformation measurements, emulsion droplet size distribution, measurement, and image of static contact angle (PDF)

■ AUTHOR INFORMATION

Corresponding Author

*E-mail: ramong@technion.ac.il

ORCID

Guy Z. Ramon: 0000-0002-0711-0654

Notes

The authors declare no competing financial interest.

■ REFERENCES

- (1) Mondal, S.; Wickramasinghe, S. R. Produced water treatment by nanofiltration and reverse osmosis membranes. *J. Membr. Sci.* **2008**, *322*, 162–170.
- (2) Fakhru'l-Razi, A.; Pendashteh, A.; Abdullah, L. C.; Biak, D. R. A.; Madaeni, S. S.; Abidin, Z. Z. Review of technologies for oil and gas produced water treatment. *J. Hazard. Mater.* **2009**, *170*, 530–551.
- (3) Vengosh, A.; Jackson, R. B.; Warner, N.; Darrah, T. H.; Kondash, A. A critical review of the risks to water resources from shale gas development and hydraulic fracturing in the United States. *Environ. Sci. Technol.* **2014**, *48*, 8334–8348.
- (4) Chakrabarty, B.; Ghoshal, A. K.; Purkait, M. K. Ultrafiltration of stable oil-in-water emulsion by polysulfone membrane. *J. Membr. Sci.* **2008**, *325*, 427–437.
- (5) Zhu, Y.; Wang, D.; Jiang, L.; Jin, J. Recent progress in developing advanced membranes for emulsified oil/water separation. *NPG Asia Mater.* **2014**, *6*, e101.
- (6) Mohammadi, T.; Kazemimoghadam, M.; Saadabadi, M. Modeling of membrane fouling and flux decline in reverse osmosis during separation of oil in water emulsions. *Desalination* **2003**, *157*, 369–375.
- (7) Zhang, L.; Zhong, Y.; Cha, D.; Wang, P. A self-cleaning underwater superoleophobic mesh for oil-water separation. *Sci. Rep.* **2013**, *3*, 23–26.
- (8) Shaffer, D. L.; Arias Chavez, L. H.; Ben-Sasson, M.; Romero-Vargas Castrillón, S.; Yip, N. Y.; Elimelech, M. Desalination and reuse of high-salinity shale gas produced water: drivers, technologies, and future directions. *Environ. Sci. Technol.* **2013**, *47*, 9569–9583.
- (9) Mueller, J.; Cen, Y.; Davis, R. H. Crossflow microfiltration of oily water. *J. Membr. Sci.* **1997**, *129*, 221–235.

- (10) Salahi, A.; Abbasi, M.; Mohammadi, T. Permeate flux decline during UF of oily wastewater: Experimental and modeling. *Desalination* **2010**, *251*, 153–160.
- (11) Chakrabarty, B.; Ghoshal, A. K.; Purkait, M. K. Cross-flow ultrafiltration of stable oil-in-water emulsion using polysulfone membranes. *Chem. Eng. J.* **2010**, *165*, 447–456.
- (12) McCloskey, B. D.; Park, H. B.; Ju, H.; Rowe, B. W.; Miller, D. J.; Freeman, B. D. A bioinspired fouling-resistant surface modification for water purification membranes. *J. Membr. Sci.* **2012**, *413–414*, 82–90.
- (13) Mcverry, B. T.; Temple, J. A. T.; Huang, X.; Marsh, K. L.; Hoek, E. M. V.; Kaner, R. B. Fabrication of low-fouling ultra filtration membranes using a hydrophilic, self-doping polyaniline additive. *Chem. Mater.* **2013**, *25*, 3597–3602.
- (14) Padaki, M.; Surya Murali, R.; Abdullah, M. S.; Misdan, N.; Moslehyani, A.; Kassim, M. A.; Hilal, N.; Ismail, A. F. Membrane technology enhancement in oil-water separation. A review. *Desalination* **2015**, *357*, 197–207.
- (15) Yang, J.; Zhang, W.; Zhang, Z.; Xu, X.; Zhu, X.; Men, X.; Zhou, X. Superhydrophilic–superoleophobic coatings. *J. Mater. Chem.* **2012**, *22*, 2834–2837.
- (16) Zhang, W.; Shi, Z.; Zhang, F.; Liu, X.; Jin, J.; Jiang, L. Superhydrophobic and superoleophilic PVDF membranes for effective separation of water-in-oil emulsions with high flux. *Adv. Mater.* **2013**, *25*, 2071–2076.
- (17) Wang, F.; Tarabara, V. V. Pore blocking mechanisms during early stages of membrane fouling by colloids. *J. Colloid Interface Sci.* **2008**, *328*, 464–9.
- (18) Faibish, R. S.; Cohen, Y. Fouling and rejection behavior of ceramic and polymer-modified ceramic membranes for ultrafiltration of oil-in-water emulsions and microemulsions. *Colloids Surf., A* **2001**, *191*, 27–40.
- (19) Wang, X.; Chen, X.; Yoon, K.; Fang, D.; Hsiao, B. S.; Chu, B. High flux filtration medium based on nanofibrous substrate with hydrophilic nanocomposite coating. *Environ. Sci. Technol.* **2005**, *39*, 7684–7691.
- (20) Yi, X. S.; Yu, S. L.; Shi, W. X.; Sun, N.; Jin, L. M.; Wang, S.; Zhang, B.; Ma, C.; Sun, L. P. The influence of important factors on ultrafiltration of oil/water emulsion using PVDF membrane modified by nano-sized TiO₂/Al₂O₃. *Desalination* **2011**, *281*, 179–184.
- (21) Wandera, D.; Wickramasinghe, S. R.; Husson, S. M. Modification and characterization of ultrafiltration membranes for treatment of produced water. *J. Membr. Sci.* **2011**, *373*, 178–188.
- (22) Tummons, E. N.; Tarabara, V. V.; Chew, J. W.; Fane, A. G. Behavior of oil droplets at the membrane surface during crossflow microfiltration of oil-water emulsions. *J. Membr. Sci.* **2016**, *500*, 211–224.
- (23) Li, H.; Coster, H. G. L.; Fane, A. G.; Vigneswaran, S. Direct observation of particle deposition on the membrane surface during crossflow microfiltration. *J. Membr. Sci.* **1998**, *149*, 83–97.
- (24) Li, H.; Fane, A. G.; Coster, H. G. L.; Vigneswaran, S. Observation of deposition and removal behaviour of submicron bacteria on the membrane surface during crossflow microfiltration. *J. Membr. Sci.* **2003**, *217*, 29–41.
- (25) Kang, S.; Subramani, A.; Hoek, E. M. V.; Deshusses, M. A.; Matsumoto, M. R. Direct observation of biofouling in cross-flow microfiltration: mechanisms of deposition and release. *J. Membr. Sci.* **2004**, *244*, 151–165.
- (26) Subramani, A.; Hoek, E. Direct observation of initial microbial deposition onto reverse osmosis and nanofiltration membranes. *J. Membr. Sci.* **2008**, *319*, 111–125.
- (27) Tummons, E. N.; Chew, J. W.; Fane, A. G.; Tarabara, V. V. Ultrafiltration of saline oil-in-water emulsions stabilized by an anionic surfactant: Effect of surfactant concentration and divalent counterions. *J. Membr. Sci.* **2017**, *537*, 384–395.
- (28) Kosvintsev, S. R.; Sutrisna, P. D.; Cumming, I. W.; Holdich, R. G.; Mason, G. The passage of deforming drops through a slotted microfilter. *Chem. Eng. Res. Des.* **2007**, *85*, 530–536.
- (29) Ullah, A.; Holdich, R. G.; Naeem, M.; Starov, V. M. Stability and deformation of oil droplets during microfiltration on a slotted pore membrane. *J. Membr. Sci.* **2012**, *401–402*, 118–124.
- (30) Darvishzadeh, T.; Tarabara, V. V.; Priezjev, N. V. Oil droplet behavior at a pore entrance in the presence of crossflow: Implications for microfiltration of oil–water dispersions. *J. Membr. Sci.* **2013**, *447*, 442–451.
- (31) Taylor, G. I. The formation of emulsions in definable fields of flow. *Proc. R. Soc. London, Ser. A* **1934**, *146*, 501–522.
- (32) Rallison, J. M. The deformation of small viscous drops and bubbles in shear flows. *Annu. Rev. Fluid Mech.* **1984**, *16*, 45–66.
- (33) Stone, H. A. Dynamics of drop deformation and breakup in viscous fluids. *Annu. Rev. Fluid Mech.* **1994**, *26*, 65–102.
- (34) Goren, S. The hydrodynamic force resisting the approach of a sphere to a plane permeable wall. *J. Colloid Interface Sci.* **1979**, *69*, 78–85.
- (35) Ramon, G. Z.; Hoek, E. M. V. On the enhanced drag force induced by permeation through a filtration membrane. *J. Membr. Sci.* **2012**, *392–393*, 1–8.
- (36) Ramon, G. Z.; Huppert, H. E.; Lister, J. R.; Stone, H. A. On the hydrodynamic interaction between a particle and a permeable surface. *Phys. Fluids* **2013**, *25*, 73103.
- (37) Falahati, H.; Tremblay, A. Y. Flux dependent oil permeation in the ultrafiltration of highly concentrated and unstable oil-in-water emulsions. *J. Membr. Sci.* **2011**, *371*, 239–247.
- (38) Li, Y. S.; Yan, L.; Xiang, C. B.; Hong, L. J. Treatment of oily wastewater by organic-inorganic composite tubular ultrafiltration (UF) membranes. *Desalination* **2006**, *196*, 76–83.
- (39) Al-Amoudi, A.; Lovitt, R. W. Fouling strategies and the cleaning system of NF membranes and factors affecting cleaning efficiency. *J. Membr. Sci.* **2007**, *303*, 4–28.
- (40) Lee, H.; Amy, G.; Cho, J.; Yoon, Y.; Moon, S. H.; Kim, I. S. Cleaning strategies for flux recovery of an ultrafiltration membrane fouled by natural organic matter. *Water Res.* **2001**, *35*, 3301–3308.
- (41) Field, R. W.; Wu, D.; Howell, J. A.; Gupta, B. B. Critical flux concept for microfiltration fouling. *J. Membr. Sci.* **1995**, *100*, 259–272.
- (42) Bacchin, P.; Aimar, P.; Field, R. W. Critical and sustainable fluxes: Theory, experiments and applications. *J. Membr. Sci.* **2006**, *281*, 42–69.
- (43) Zhong, H.; Yang, L.; Zeng, G.; Brusseau, M. L.; Wang, Y.; Li, Y.; Liu, Z.; Yuan, X.; Tan, F. Aggregate-based sub-CMC solubilization of hexadecane by surfactants. *RSC Adv.* **2015**, *5*, 78142–78149.